Collision of monopoles, disclinations and dislocations

Pawel Pieranski, Maria Helena Godinho

Collisions of monopoles, disclinations and dislocations

Pawel Pieranski and Maria Helena Godinho

Abstract

Motions and collisions of topological defects produced during symmetry breaking transitions is a crucial issue in cosmology and in condensed matter physics. Here, we deal with topological defects in nematics and cholesterics. Nematics may contain linear defects *i.e.* disclinations and point defects *i.e.* monopoles while cholesterics may contain linear defects of their 1D periodic order parameter, *i.e.* dislocations. The dowser texture appears as a natural universe of the nematic monopoles. They can be generated in it, set into motion and brought to collisions that may result in annihilation of pairs of monopoles. We show how to generate pairs of disclinations in twisted nematic cells by the isotropic-nematic transition in the presence of magnetic fields. When two such disclinations collide, *i.e.* enter into a contact at one point, an intercommutation or rewiring into a new pair of disclination can occur. We show how to bring these disclinations to collisions by means of an electric field and how to steer the rewiring by magnetic fields. For generation of dislocations in cholesteric we use a Grandjean-Cano wedge made of crossed cylindrical mica sheets. After their nucleation upon dilation, dislocation loops are growing and collide. Collision of dislocation loops can result in a trivial crossing or may produce a stable configuration called Lehmann cluster. Subsequently, upon application of a high enough tensile strain, the Lehmann splits into a pair of dislocations that can be entangled.

1 Introduction

Motions and collisions of topological defects produced during symmetry breaking transitions is a crucial issue in cosmology and in condensed matter physics [1, 2, 3]. Here, we deal with topological defects in nematics and cholesterics.

Nematic may contain linear defects *i.e.* disclinations (see Fig.1a-c) and point defects *i.e.* monopoles (see Fig.1d-f) while cholesterics may contain linear defects of their 1D periodic order parameter, *i.e.* dislocations (see Fig.1g-h).

In a cholesteric with the full pitch p (corresponding to the 2π rotation of the director along the helix axis) two types of dislocations are possible. Those with the Burger vector $b = p/2$, called *single* or *thin*, have a singular core and therefore are equivalent to disclinations in nematics. In this paper we deal only with dislocations of the second type called *double* or *thick* with the Burgers vector $b = p$ and characterized by the director field that can be fully continuous, without singularities (see Fig.1h).

Monopoles that have singular point-like cores move on 1D linear trajectories $\mathbf{r}(t) = [x(t), y(t), z(t)]$. One could think therefore that the collision of two monopoles occurs when their trajectories reach the same point at the same time : $\mathbf{r_1}(t) = \mathbf{r_2}(t)$. We will show below that in reality one can speak about the collision of two monopoles when the distance between them $|\mathbf{r_1}(t) - \mathbf{r_2}(t)|$ becomes smaller than a characteristic distance λ that depends like $1/v$ on the velocity v of their motion (let us note an analogy with the de Broglie wave length $\lambda \sim 1/v$). We will show that in certain cases annihilation of the colliding pair can occur.

The collision of two disclinations occurs when their linear cores come into intersection. In such a case rewiring (or intercommutation) of disclinations can occur.

The collision of two double dislocations is less evident to define because they don't have singular cores. In spite of that the double dislocations appear in a microscope as well defined thick lines. In this situation, one can speak about the collision of when the distance between two such lines becomes smaller than the size of their director field p. We will show that in certain cases, collision of two dislocations can result in their rewiring like in the case of disclinations.

However, in the case depicted in Fig.1h, collision of the two coplanar dislocations leads to formation a low energy state called *Lehmann cluster* having the D_2 symmetry. When submitted to high enough tensile strain, the Lehmann cluster splits into a pair of two non-coplanar dislocations and the D_2 symmetry is broken into C_2. We will show that the $D_2 \rightarrow C_2$ symmetry breaking results in generation of *tangles of dislocations* which can be seen as *topological metadefects i.e.* defects made of topological defects.

2 Generation, motion and collisions of monopoles

Monopoles are by far less frequent in nematics than disclinations [2, 3]. In particular, they do not appear spontaneously during the Isotropic ⇒ Nematic first order transition for a topological reason. Indeed, the 3D director field $\mathbf{n}(\mathbf{r})$ surrounding one monopole maps onto the whole unit sphere that is to say it covers twice the order parameter space of nematics corresponding to one hemisphere (see Fig.1d-f). Probability

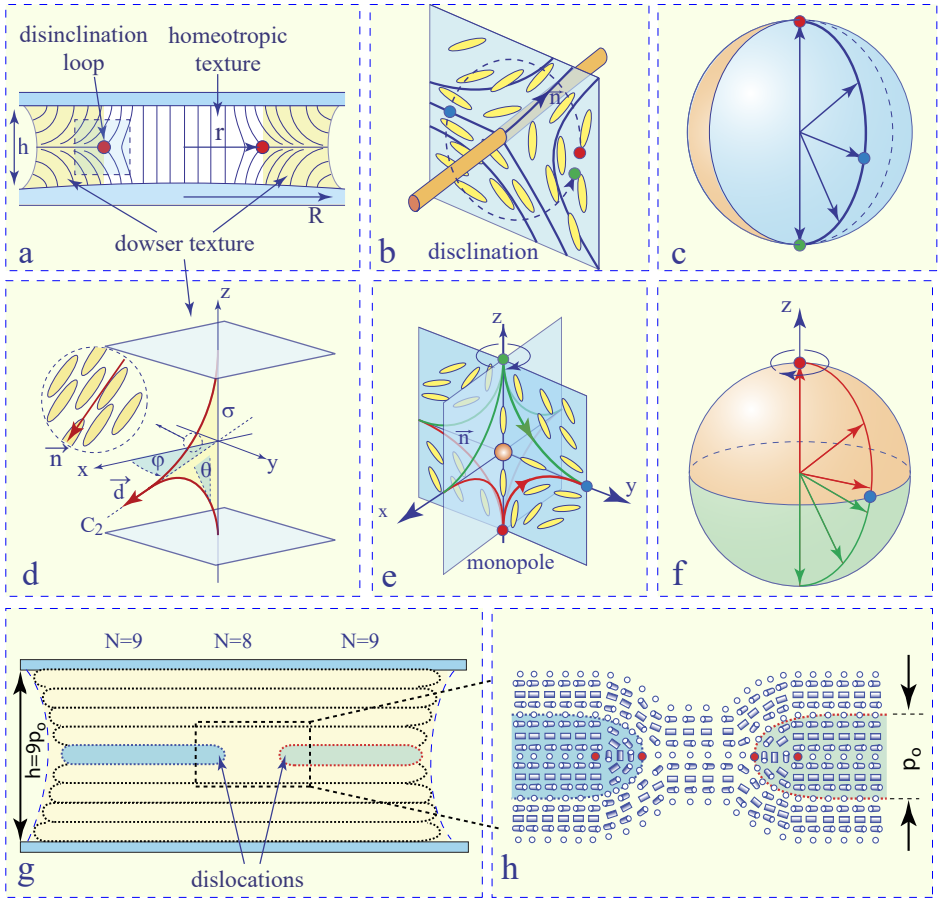

Figure 1: Topological defects. a-c) Disclination. d-f) Monopole. g-h) Dislocation. a) Director field inside a nematic droplet confined between surfaces (lens, glass slide and meniscus) imposing the homeotropic anchoring. For topological reasons it contains the disclination loop. b) Director field in the vicinity of the disclination. c) Mapping of the director field from the dotted circle surrounding the disclination on one meridian of the space of the nematic order parameter. d) Director field of the dowser texture. e) Director field in the vicinity of the monopole. f) The director field surrounding the monopole mapped on the space of the nematic order parameter covers it twice. g) Cholesteric layer confined between surfaces with planar anchoring conditions. Dislocations separate areas with N=9 and N=8 full cholesteric pitches. h) Director field of dislocations.

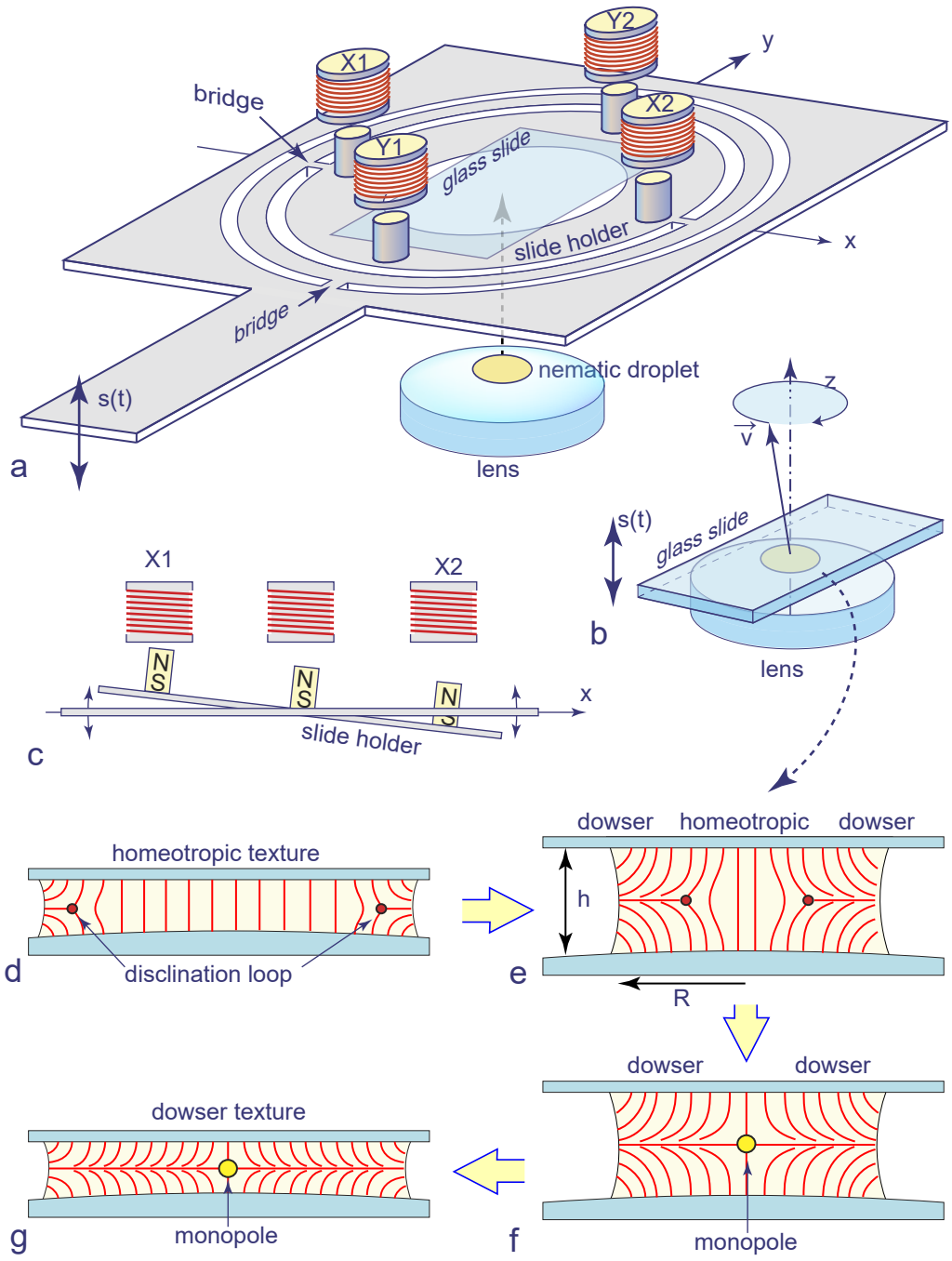

Figure 2: Setup for generation and winding of the dowser texture in nematics : a) Perspective view of the setup called Circular Dowsons Collider. b) Perspective view of the nematic droplet confined by capillarity between the glass slide and the lens. c) Side view of the glass slide holder. d) The ground state texture of the nematic droplet confined between surfaces with homeotropic anchoring conditions. The peripheral dislocation loop is due to the homeotropic boundary conditions at the nematic/air interface. d-f) When the ration h/R is larger than 1, the dislocation loop shrinks and collapses. As a result, the homeotropic texture is replaced by the dowser texture and the monopole is created. g) The dowser texture persists until the thickness h is reduced almost to zero.

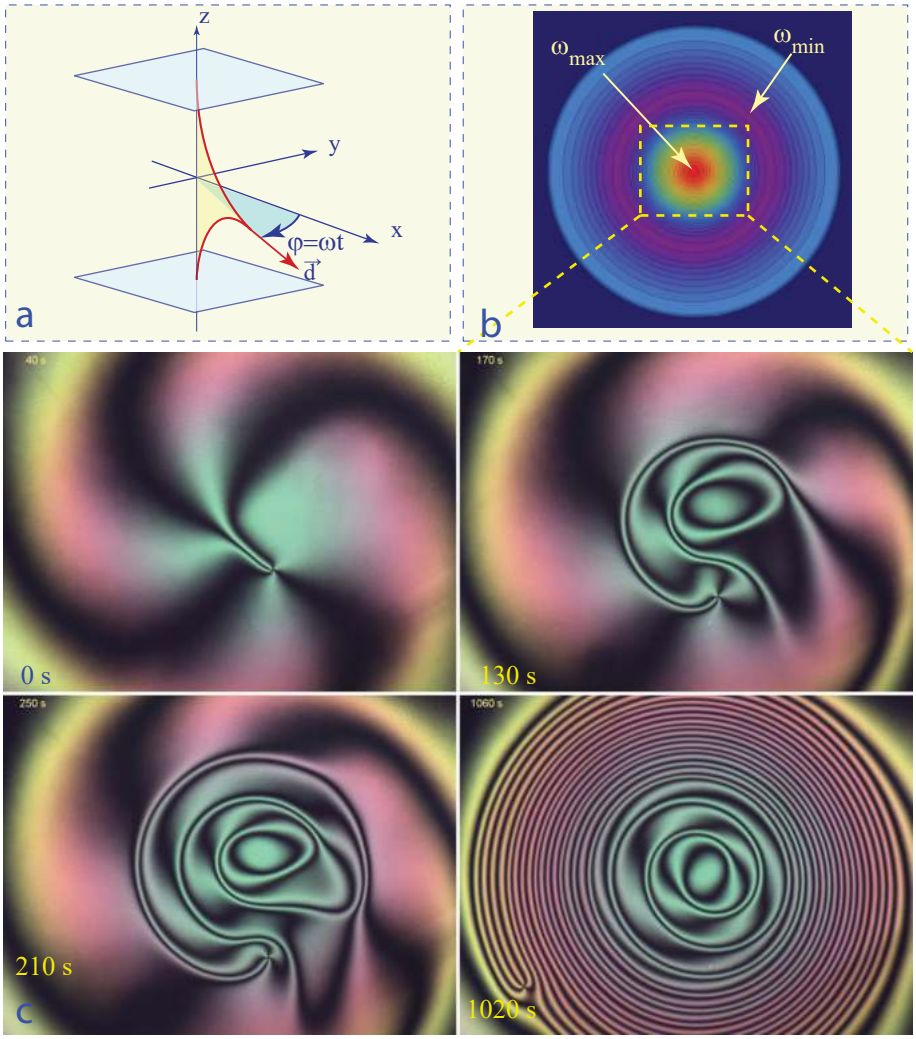

Figure 3: Winding of the dowser texture in the Circular Dowsons Collider. a) Definition of the azimuthal angle φ. b) Variation of the angular velocity $\omega = d\varphi/dt$ with the distance r from the centre. c) Experiment. Winding process illustrated with pictures taken in polarised light. (see video *Winding dowser texture* in Supplementary Material)

of a spontaneous generation of such a complex configuration of the director field in bulk during the Isotropic ⇒ Nematic transition in bulk is negligible.

Generation of monopoles requires thus some deliberate manipulation of the director field for example through adequate boundary conditions and flows. In practice, as we will show below, monopoles can be easily generated in the so-called dowser texture in which the director $\mathbf{n} = (sin\theta cos\varphi, sin\theta sin\varphi, cos\theta)$ with $\theta = \pi z/h$ rotates by π between limit surfaces located at $z = \pm h/2$ and equipped with homeotropic anchoring conditions ($\mathbf{n}\|\mathbf{z}$) ((see Fig.1d). When mapped onto the unit sphere, the director field of a uniform dowser texture covers one meridian of the longitude φ (see Figs.1e-f). Let us note that the dowser texture is symmetrical with respect to two elements: the mirror plane σ and the twofold axis C_2. For this reason, the order parameter of the dowser texture is the 2D *vector* field $\mathbf{d}$ called the dowser field.

Special setups, called dowsons colliders, were developed for generation of nematic monopoles and for driving them into motions that lead to their collisions. They are extensively discussed in recent references [4] and [5, 6].

2.1 Generation of monopoles in the dowser texture

In all of them, a nematic droplet (5CB) or radius R is hold by capillarity in the gap of thickness h between a glass slide and a lens (see Fig.2a and b). Glass surfaces treated with egg yolk provide homeotropic anchoring conditions (director $\mathbf{n}$ orthogonal to the surface) so that in the ground state the director field has a vertical uniform orientation (homeotropic director field) except for the vicinity of the meniscus where the homeotropic anchoring at the nematic/air interface perturbs the director field $\mathbf{n}$ as shown in Fig.2d. For topological reasons the perturbed field contains one dislocation loop close to the meniscus.

Generation of nematic monopoles proceeds in three steps. During the first step the homeotropic texture is transformed into the dowser texture. For this purpose the glass slide is moved up and the slide/lens gap is increased until the ratio h/R reaches the critical value of ≈ 1 (see Fig.2e). In these conditions, for energetical reasons [5, 6], the dislocation loop shrinks and collapses into the monopole as shown in Fig.2f. By this means the whole drop is filled now with the distorted dowser texture in which the director rotates by π between the glass surfaces. When the thickness h of the lens/slide gap is reduced subsequently almost to zero, the dowser texture persists in spite of its metastability with respect to the homeotropic texture because the reverse *dowser* → *homeotropic* transition is protected by a high energy barrier of generation of the disclination loop.

The second steps consists in winding up the dowser texture. For this purpose the glass slide, fixed on its flexible support (see Fig.2a) is set into a conical motion as shown in Fig.2b which drives rotation of the dowser field $\mathbf{d}$ around the axis z. The angular velocity of the dowser field (much smaller than that of the conical motion) is maximal at the center of the lens/slide gap and decreases with the radial distance r from it. As a result one obtains a texture in which the azimuthal angle φ varies with radius r (see Fig.3). Such a wound up dowser texture can be seen as a spiral shaped 2π wall across which field the azimuthal angle (the longitude) φ rotates by 2π as $\varphi = qr$ with $q = 2\pi/\lambda$. The director field of the 2π wall covers the whole unit sphere.

Monopoles are produced during the third step (see Figs.4 and 5) during which a fast enough transitory Poiseuille flow breaks the 2π walls and generate pairs of $+2\pi$ and -2π point defects of the dowser field $\mathbf{d}$ which are nothing else but nematic monopoles. For obvious reasons the monopoles generated in the dowser texture were dubbed "dowsons d+ and d-" (see Fig.5c). As dowsons generated by this method are located at extremities of the broken 2π walls, they are set into motion by the tension of walls (energy per unit length). The resulting shortening of walls involves the viscoelastic relaxation of the dowser field. In other words one can say that dowsons are "pulled" by the tension of the broken 2π walls.

Let us stress again that, as shown in Figs.5e and f, the dowsons d- and d+, seen in three dimensions (x,y,z), are nematic monopoles. Remarkably, in Figs.5e and f the dowsons d- and d+ have the same hyperbolic configuration of the director field but they differ by orientation of the axis of their revolution symmetry: it parallel to y in Fig.5e and to x in Fig.5e.

Motions of the monopoles driven by the shortening of the 2π walls bring them to collisions. In the field inside the dotted circle in Figs.5c-i, collisions of pairs (d+d-) of dowsons, i.e. pairs of monopoles, leads to their annihilation. On the contrary, the annihilation is avoided during the collision of the pair of dowsons inside the dotted rectangle in Figs.5c-g; after the collision the distance between the dowsons increases. It can be shown (see refs.[5, 6]) that the cross section for anninhilation of dowsons pairs is $\lambda/2$.

3 Collisions and intercommutation of disclinations

3.1 Principle

It is well known that when two disclination lines collide, *i.e.* enter into a contact at one point C, intercommutation [3] or equivalently, rewiring [7, 8, 9, 10] of the two disclinations into a different pair of disclinations can occur.

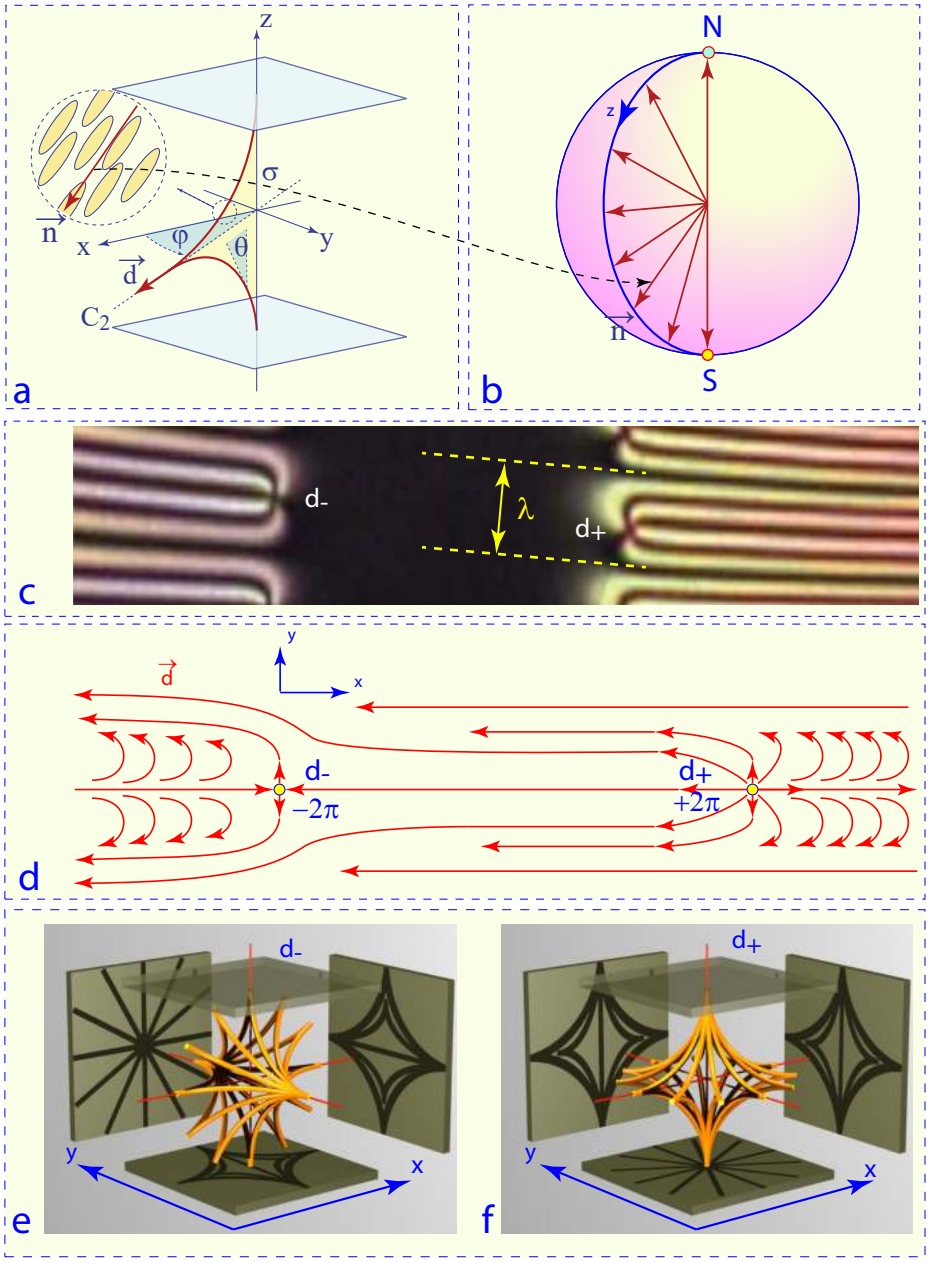

Figure 4: Generation of monopoles in nematics : a) The director field of the dowser texture. b) Mapping of the dowser texture onto one meridian in the space of the nematic order parameter. c-f) Dowsons d+ and d-, the $+2\pi$ and -2π point defects of the dowser field **d**, are monopoles of the director field **d** in a 3D nematic. c) View in the polarising microscope of a wound up dowser field containing pairs of dowsons d+ and d- generated by breaking of 2π walls. d) Dowser field in the presence of the (d+d-) pair. e-f) View of the 3D director fields in vicinity of nematic monopoles corresponding to dowsons d+ and d-. Let us stress that topologically the two fields are identical but they differ by their orientations with respect to the limit surfaces.

Figure 5: Generation, motions and collision of monopoles. a) View of a wound up dowser texture in a polarised light. b) Breaking of 2π walls by a transitory Poiseuille flow. c-i) Field inside the dotted circle: collisions of dowsons pairs d+ and d- leading to their annihilation. c-f) Field inside the dotted rectangle: avoidance of annihilation during collision of a dowsons pair. (see video *Collisions monopoles* in Supplementary Material)

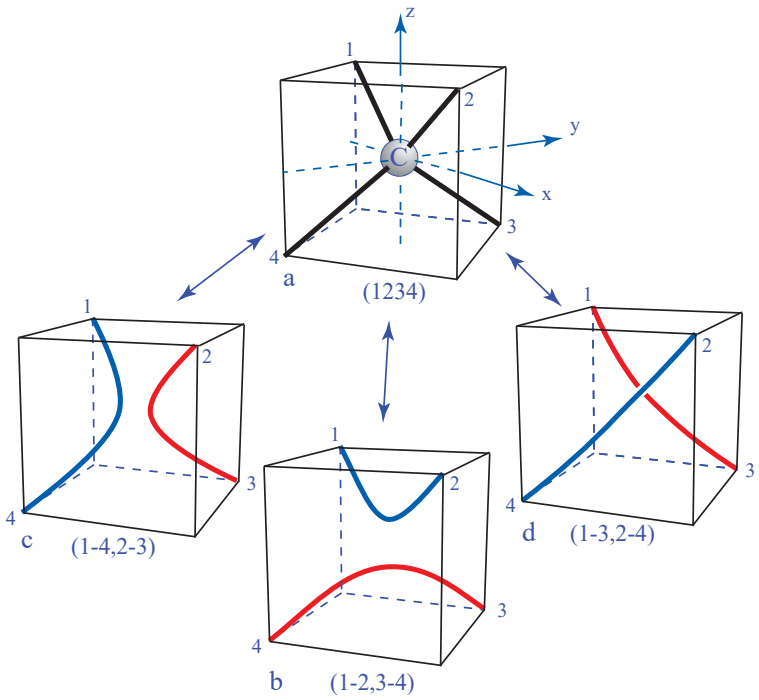

Figure 6: General principle of the intercommutation of colliding disclinations. a) Configuration (1234): four disclination lines meet at the point C. b,c,d) Three possible configurations (1-2,3-4), (1-4,2-3) and (1-3,4-2) resulting from the (1234) state by connections of the four disclinations into two pairs of disclinations. Remark: the cubic geometry in these schemes has no importance. Only the topology of disclinations matters.

One can consider this problem from a little different, more general point of view by starting from the contact state (Fig.6a) in which four lines 1, 2, 3 and 4 meet at the point C. This contact state (1234) is in general unstable and evolves into one of the three possible reconnections of the four disclinations into pairs represented in Figs.6b, c and d: (1-2,3-4), (1-3,2-4) and (1-4,3-2). Let us stress that any intercommutation between these paired states must involve a passage through the contact state.

Collisions leading to intercommutation of disclinations can occur in several circumstances represented schematically in Fig.7.

1. A rapid quench from the isotropic to the nematic state generates a random tangle of disclinations [2, 3] (Fig.7a). Its subsequent evolution, driven by elasticity, involves shortening of disclination loops as well as intercommutation events during collisions of disclinations' segments at their crossing.
2. In the presence of colloidal inclusions, the tangle of disclinations is structured into loops and/or knots. In Fig.7b the intercommutation occurs at the crossings of two independent loops [7, 8, 9, 10].
3. Disclinations loops can be produced, stretched and brought into collisions by flows in microfluidic systems as shown in Fig.7d [11].
4. Disclination loops captive on polymeric fibers can be brought into collisions by action of magnetic fields. In Fig.7d the intercommutation occurs at the contact point of two adjacent loops [12].
5. In Fig.7e two disclinations, stretched between glass slides, can be brought into a collision by a relative translation of the slides [1].
6. In this paper we deal with disclinations in twisted nematic cells (Fig.7f). We will show how such disclinations can be generated and brought into collision in a controlled manner. Moreover, we will also show how all possible intercommutation processes listed in Fig.6 can be explored.

3.2 Setup

Experiments presented here have been performed for the first time with a twisted nematic display built for a pedagogical purpose [13]. Its construction is a classical one. Two glass slides equipped with ITO electrodes were first coated with a thin layer of PVA and then buffed with a velvet fabric. Finally, the slides were assembled with crossed anchoring directions by means of 40μm mylar spacers and of an epoxy glue. The cell was filled by capillarity with 5CB. Let us note that for a pedagogical purpose, the letter "M" was beforehand etched in one of the ITO electrodes.

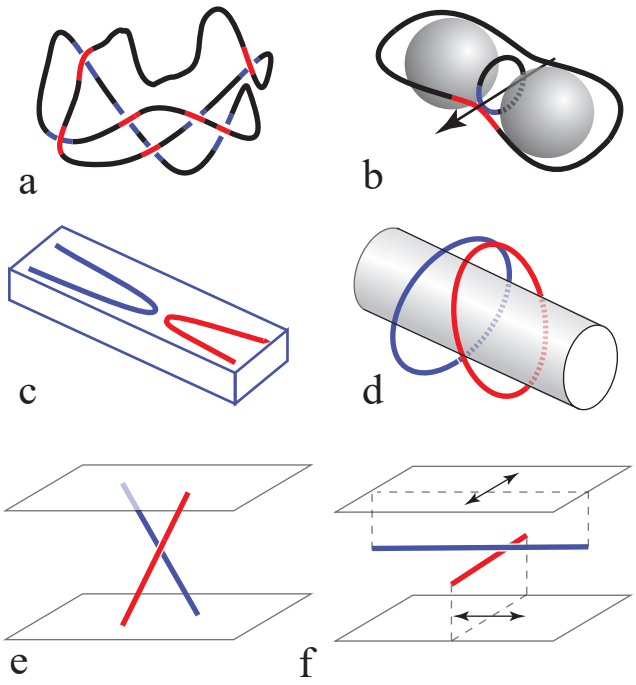

Figure 7: Geometries of experiments on collisions of disclinations leading to the intercommutation. a) Entangled disclinations generated at random by the isotropic → nematic quench. b) Disclinations associated with colloidal inclusions. c) Disclinations in microfluidic channels. d) Disclination loops captive on fibers. e) Disclinations stretched between parallel surfaces. f) Disclinations in twisted nematic cells studied here. In the presence of an electric field larger than the threshold of the Fréedericksz transition they are located at different levels.

3.3 Generation and shapes of disclinations

It is well known that two configurations of the director field of opposite helicities R and L :

$$\mathbf{n}_R = [\cos(\pi z/h), \sin(\pi z/h)] \tag{1}$$

and

$$\mathbf{n}_L = [\cos(\pi z/h), -\sin(\pi z/h)] \tag{2}$$

are possible in twisted cells (see Fig.8c). For topological reasons they must be separated by disclination lines. In our experiments disclinations were generated by the isotropic→nematic transition which in twisted cells breaks the mirror symmetry with respect to (x,z) and (y,z) mirror planes.

In the absence of perturbations, the R and L domains resulting from this mirror symmetry breaking are generated at random. However, when a magnetic field $\mathbf{B}$ is applied to the twisted cell during the isotropic→nematic transition, the choice of the helicity is influenced by the direction of the horizontal component $\mathbf{B}_\perp(\mathrm{B}_x,\mathrm{B}_y)$ of the magnetic field.

Let ψ be the angle between $\mathbf{B}_\perp$ and the x axis (see Fig.8b). When $0 < \psi < \pi/2$ or $\pi < \psi < 3\pi/2$, the right helicity R of the twisted director field is favoured for energetical reasons. Otherwise, for $\pi/2 < \psi < \pi$ or $3\pi/2 < \psi < 2\pi$, the left helicity is selected. This selection rule opens the way for a controlled generation of helicities patterns and of the corresponding disclinations' nets.

In the experiment represented in Fig.8a, an annular neodymium magnet was located on the upper slide of the twisted cell. Its field $\mathbf{B}_\perp$ is radial with respect to the magnet symmetry axis z. In terms of the selection rule stated above, the expected pattern of the R and L domains should have the quadrant geometry and disclinations should be parallel to the x and y axes.

For an arbitrary field $\mathbf{B}_\perp$ stable positions of the disclination lines can be determined, in the limit of small fields, through calculation of magnetic energies per unit area of the right and left handed helices $n_R(z)$ and $n_L(z)$. As the anisotropic part of the magnetic energy density writes

$$f_{mag} = -\frac{1}{2}\frac{\chi_a}{\mu_o}(\mathbf{n}\cdot\mathbf{B})^2 \tag{3}$$

with $\chi_a = \chi_{//} - \chi_\perp$, one obtains the difference in magnetic energies by integration on z:

$$\Delta F_{mag} = -\frac{1}{2}\frac{\chi_a}{\mu_o}\int_0^h \left[(\mathbf{n}_L\cdot\mathbf{B})^2 - (\mathbf{n}_R\cdot\mathbf{B})^2\right] dz = \frac{\chi_a}{\mu_o} B_x B_y \tag{4}$$

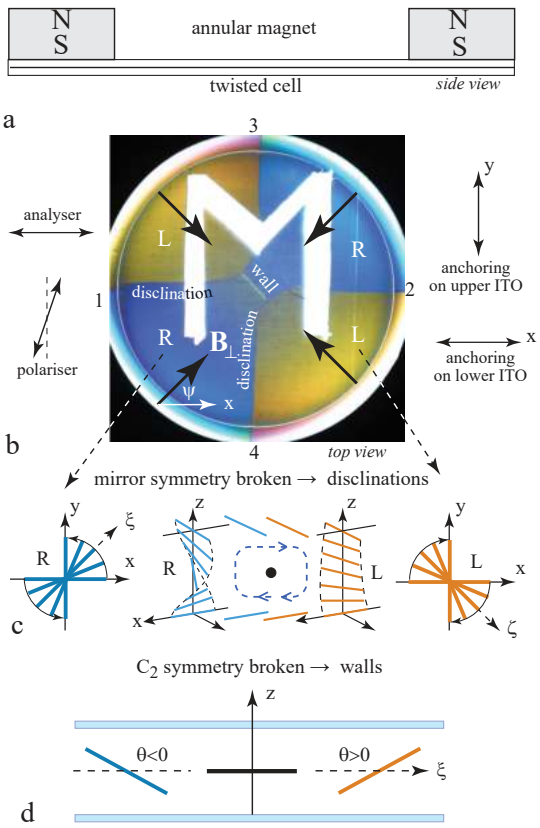

Figure 8: Principle of the experiment on collisions of disclinations in twisted nematic cells. a) Side view of a twisted nematic display submitted to the action of an annular magnet. b) Top view of the display between slightly decrossed polarisers unveils the presence of four sectors with the left (L) or right (R) helicities of the twisted director field. They are generated by the magnetic field $\mathbf{B}$ of axial symmetry with respect to the z axis. c) For topological reasons, domains with left and right helicities are separated by disclinations. d) Upon application of an electric field larger than the threshold E_c of the Fréedericksz transition, walls are generated. Their positions are controlled by the geometry of the magnetic field. In particular, due to vanishing of the $\mathbf{B}_\perp$ component of the magnetic field, a short wall is generated in the R domain at the magnet centre. In Fig.9 we show that this wall exerts a traction on disclinations and brings them into a collision when the electric field is strong enough. The second, circular wall is due to vanishing of the $\mathbf{B}_z$ component of the magnetic field.

Therefore, stable positions of disclination lines correspond to solutions of the equation

$$G_d(x,y) = B_x(x,y)B_y(x,y) = 0 \tag{5}$$

In the case of the annular magnet, the generic function $G_d(x,y)$, calculated in the approximation of a ring of magnetic dipoles, is represented in Fig.9a. In agreement with qualitative considerations above, its zero level lines coincide with the x and y axes.

The experimental result shown in Fig.9a is slightly different: instead of straight disclination lines, labeled 1-2 and 3-4, crossing in the centre of the annular magnet, two curved disclinations labeled 1-3 and 2-4 are present here. In terms of the intercommutations' scheme of Fig.6, this pattern corresponds to the configuration (1-3,2-4) of Fig.6d.

This disagreement is only apparent because the selection rule stated above was obtained without taking into account the energy of disclinations proportional to their length. Obviously, the total length of curved disclinations 1-3 and 2-4 is smaller then that of straight disclinations 1-2 and 3-4 crossing in the centre.

3.4 Generation and shapes of walls

Upon application of an electric field larger then the threshold of the Fréedericksz transition, the domains with R and L helicities become coloured (see Fig.9b). These colors depend on the tilt angle θ and vary when the intensity of the electric field changes.

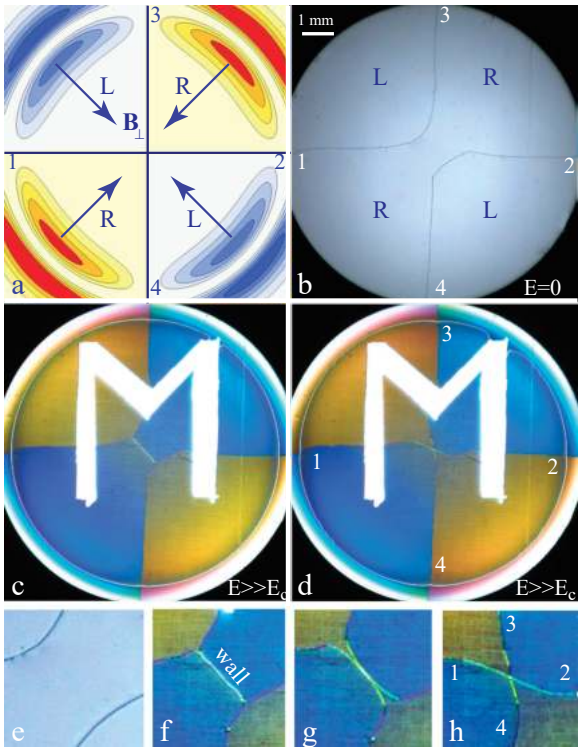

Figure 9: Generation of disclinations and walls conditioned by the geometry of the magnetic field of the annular magnet. a) Radial magnetic field $\mathbf{B}_\perp$ and the generic function $D(x,y) = B_x B_y$ calculated in the approximation of a dipolar ring. b) Disclinations generated by the isotropic-nematic transition in the presence of the magnetic field of the annular magnet (E=0, crossed polarisers). c) Fréedricksz transition. Domains with R and L helicities become coloured when observed between slightly decrossed polarisers. Note the presence of a white line in the center of the blue (R) domain. This is the wall separating domains with positive and negative tilt angles θ defined in Fig.8d. The shrinking wall pulls on the disclination lines and leads to their collision. d) Collision of disclinations results in an intercommutation process: the initial configuration (1-3,2-4) is replaced by the (1-2,3-4) one. e-h) Closeups of the central part of pictures a-d.

For the purpose of the forthcoming discussion it is important to note the presence of a white line in the center of the blue (R) domain. This is the wall separating domains with positive and negative tilt angles θ defined in Fig.8d. Its location in the centre is not accidental but, on the contrary, it is imposed by the geometry of the magnetic field generated by the annular magnet. Indeed, the magnetic field which is vertical on the magnet axis z, becomes tilted in its vicinity. This position-dependent tilt of the magnetic field imposes the choice of the sign of the angle θ and by this means generates the wall.

Let us note that beside this central short wall connecting disclinations 1-3 and 2-4, there is a second, circular wall. This second wall is also imposed by the geometry of the magnetic field. It is located on the circle on which the magnetic field is horizontal, B_z=0.

For an arbitrary magnetic field, stable positions of walls in fields with right and left handed helices correspond to zeroes of the generating functions

$$G_{wR}(x,y) = B_\xi B_z = 0 \quad and \quad G_{wL}(x,y) = B_\zeta B_z = 0 \tag{6}$$

involving B_ξ and B_ζ components of the magnetic field along the ξ and ζ bisectrix axes defined in Fig.8c.

3.5 Intercommutation of colliding disclinations

When the electric field is strong enough, the central wall shortens (see Figs.9c and g) and pulls on the two disclinations connected by it. Finally, it brings them into a collision (see Figs.9d and h). As a result an intercommutation of disclinations occurs: the configuration (1-3,2-4) is replaced by the (1-2,3-4) one.

This first observation of the intercommutation process was followed by a systematic study illustrated by the series of 20 pictures in Fig.10 which were taken at a larger magnification.

Experiments start with the configuration (1-2,3-4) represented in more details in Fig.10a'. It is similar to a collisionless two-level crossing of roads: the disclination 1-2 is situated above the dislocation 3-4. This is well visible in the picture a focussed on the disclination 3-4 which appears as a sharp black line

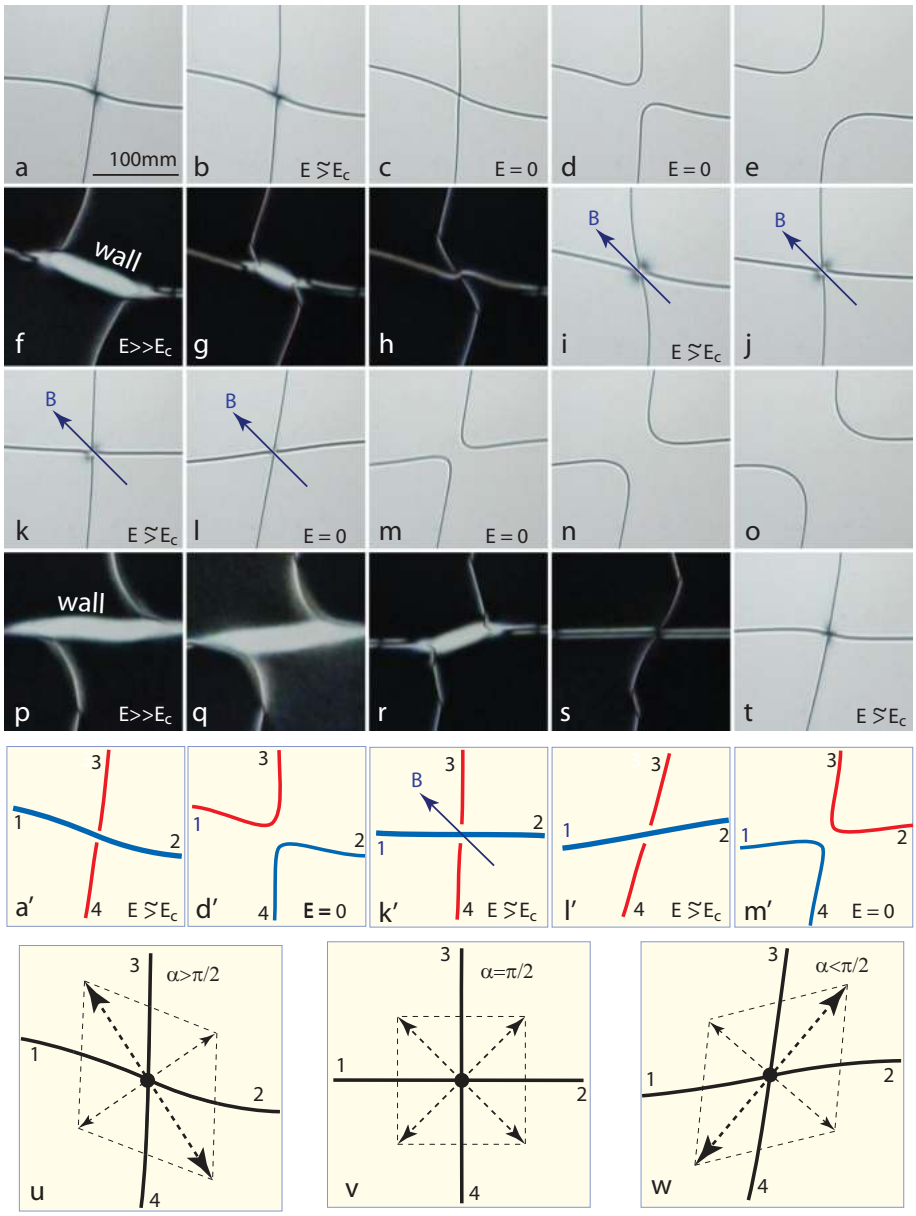

Figure 10: Intercommutations of colliding disclinations. a,a',b) Configuration (1-2,3-4) defined in Fig.6b. c) Configuration (1234) defined in Fig.6a is obtained from (1-2,3-4) by switching off the electric field. c,d,e) Instability of the one-level crossing results in the intercommutation (1234)→(1-3,2-4). It is driven by the inequality 7. f-i) Restoration of the initial configuration (1-2,3-4) driven by a strong electric field. It follows the path (1-3,2-4)→(1234)→ (1-2,3-4). i-l) Modification of the angle α driven by the horizontal magnetic field. e-o) Two-stage intercommutation (1-2,3-4)→(1234)→(1-4,2-3) driven by the reversed inequality 7. a',d',k',l',m') Schematic representations of disclinations in pictures a,d,k,l,m. u) Inequality 7 of forces acting on the one-level crossing (1234). v) The marginal case of an unstable equilibrium. w) Reversed inequality 7 of forces acting on the one-level crossing (1234). (see video *Rewiring Crossing Disclinations* in Supplementary Material)

(between crossed polarisers) while the disclination 1-2 being of the focus appears as a slightly larger line. This (1-2,3-4) configuration is stable when the electric field is larger than the threshold of the Fréedericksz transition.

The first intercommutation of disclinations is triggered by suppressing the electric field. When E is set to zero, disclinations 3-4 and 1-2 move respectively up and down and finally collide at mid-height of the cell at z=0 level (picture c). The (1234) configuration created by this means (see Fig.10c) is unstable so that the intercommutation into the configuration (1-3,2-4) occurs as shown in Figs.10d and d'.

At this stage of experiments one can ask why this second intercommutation process lead to the configuration (1-3,2-4) and not to the (1-4,2-3) one which is also possible in terms of our general scheme in Fig.6. So far we ignored the detailed structure of the the one-level crossing Fig.10c produced by the collision of disclinations 1-2 and 3-4. Nevertheless one can say that it is submitted to four forces - tensions $\mathbf{t}_1$,...$\mathbf{t}_4$ of the four disclination lines - which are represented schematically in Fig.10u. Composition of these forces, two-by-two, shows that

$$|\mathbf{t}_1 + \mathbf{t}_3| = |\mathbf{t}_2 + \mathbf{t}_4| > |\mathbf{t}_1 + \mathbf{t}_4| = |\mathbf{t}_2 + \mathbf{t}_3| \tag{7}$$

so that the intercommutation (1234)→(1-3,2-4) is favoured. Obviously this inequality is determined by the value of the angle α which is larger than $\pi/2$. Therefore, for α smaller than $\pi/2$ the inequality 7 should be reversed and the intercommutation (1234)→(1-4,3-4) should be favoured.

With the aim to test this conjecture, we had to produce one-level crossings (1234) with different angles α. For this purpose we applied first a strong electric field $E \approx 4E_c$ to the configuration (1-3,2-4) shown in the picture e. As discussed above, a wall pulling on the two disclinations appeared. Its shortening lead to the collision shown in the picture h and to the intercommutation (1234)→(1-2,3-4). Subsequently, the intensity of the electric field was lowered to $E \approx 1.2E_c$ and a horizontal magnetic field $\mathbf{B}$ was applied in the diagonal direction (ζ defined in Fig.8c) as shown in pictures i-l and k'. Such a field favors the left helicity of the twisted texture [15] (see Fig.8c) so that the angle α decreases to a value smaller than $\pi/2$ (see pictures l, l' and w).

After this restoration of the (1-3,2-4) configuration with $\alpha < \pi/2$, the electric field was switched off so that the intercommutation (1-3,2-4)→(1234) occurred. Following our conjecture, the scheme of the line tensions acting on the one-level crossing (1234) shown in the picture w favors the intercommutation (1234)→(1-4,3-2). The series of four pictures l-o proves that the conjecture is confirmed.

The last five pictures p-t show that the initial configuration (1-2,3-4) can be easily restored by application of a strong enough electric field.

Using the horizontal magnetic field of appropriate direction we tested our conjecture with many different values of the angle α. In the marginal case of $\alpha \approx \pi/2$ the choice between intercommutations (1234)→(1-4,3-2) and (1234)→(1-3,2-4) was random.

3.6 Discussion and conclusions

As stated in the introduction, collisions of disclinations resulting in their intercommutations have been observed previously in several geometries but a method allowing a controlled production of the all three possible intercommutation processes (defined in Fig.6) in a reversible manner was missing. The work presented here filled this gap but at the same time opened new challenging issues.

First of all, the detailed structure in the centre of the (1234) configuration (defined in Fig.6a) resulting from a collision of two disclination lines is unknown. Is it a one-level flat crossing or a three-dimensional one?

In all experiments we made, the (1234) configuration appeared as short-lived *i.e.* unstable with respect to one of the three possible intercommutations defined in Fig.6. However, one can still ask if in the marginal case of $\alpha = \pi/2$ the (1234) configuration could be only metastable.

Due to the slab-like geometry of the twisted nematic cell, the configuration (1-2,3-4), similar to a two-level road crossing, is different from the other two. In our classical twisted nematic cell, it is stable only in the presence of an electric field larger than E_c. In this context we should emphasize that Wang, Li and Yokoyama [16] ware able to stabilise a square-shaped web of disclinations by means of judicious anchoring patterns on limit surfaces. All crossings in this web have the (1-2,3-4) configuration. Is it possible to bring these crossing disclinations into collisions by action of electric fields?

Collisions of disclinations in nematic colloids lead also to intercommutation processes which in this context are rather known as rewiring processes. They are reviewed by Muševič in ref.[10]. We hope that our work can shed a new light on this exceptionally rich systems in which the nematic matrix is multiply connected.

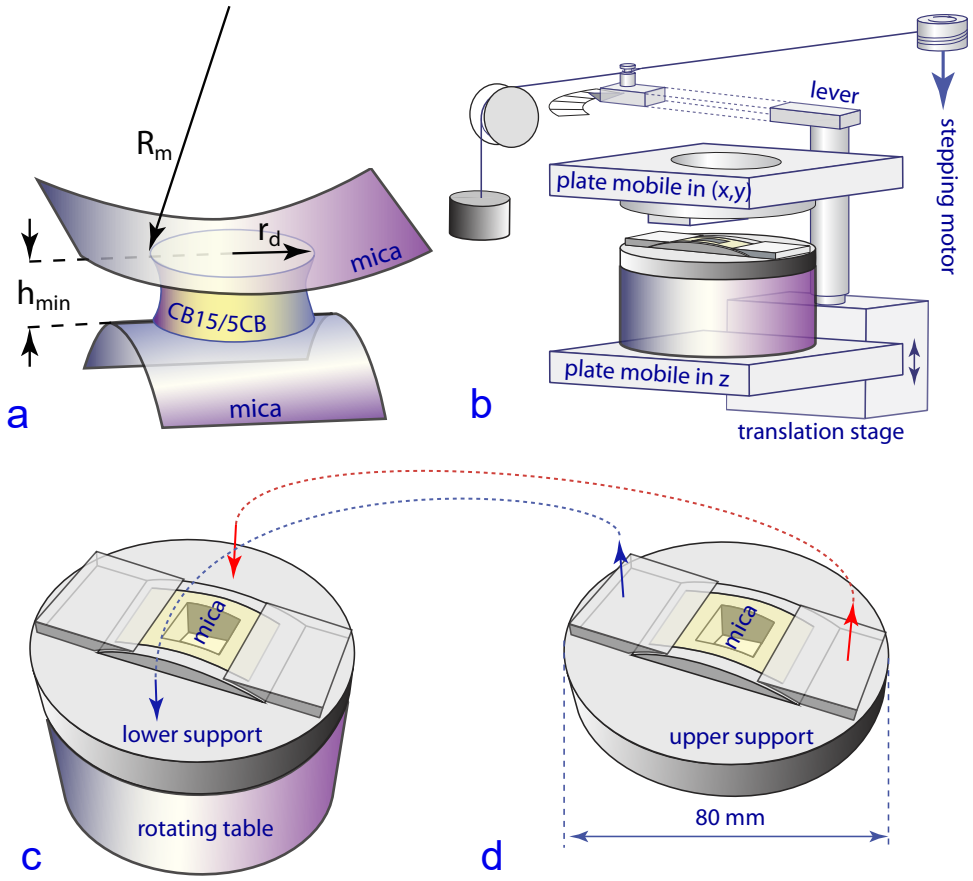

Figure 11: Setup for nucleation and observation of dislocations in cholesterics. a) Geometry of the cylinder/cylinder gap. b) Perspective view of the setup. c and d) Lower and upper supports of the mica sheets.

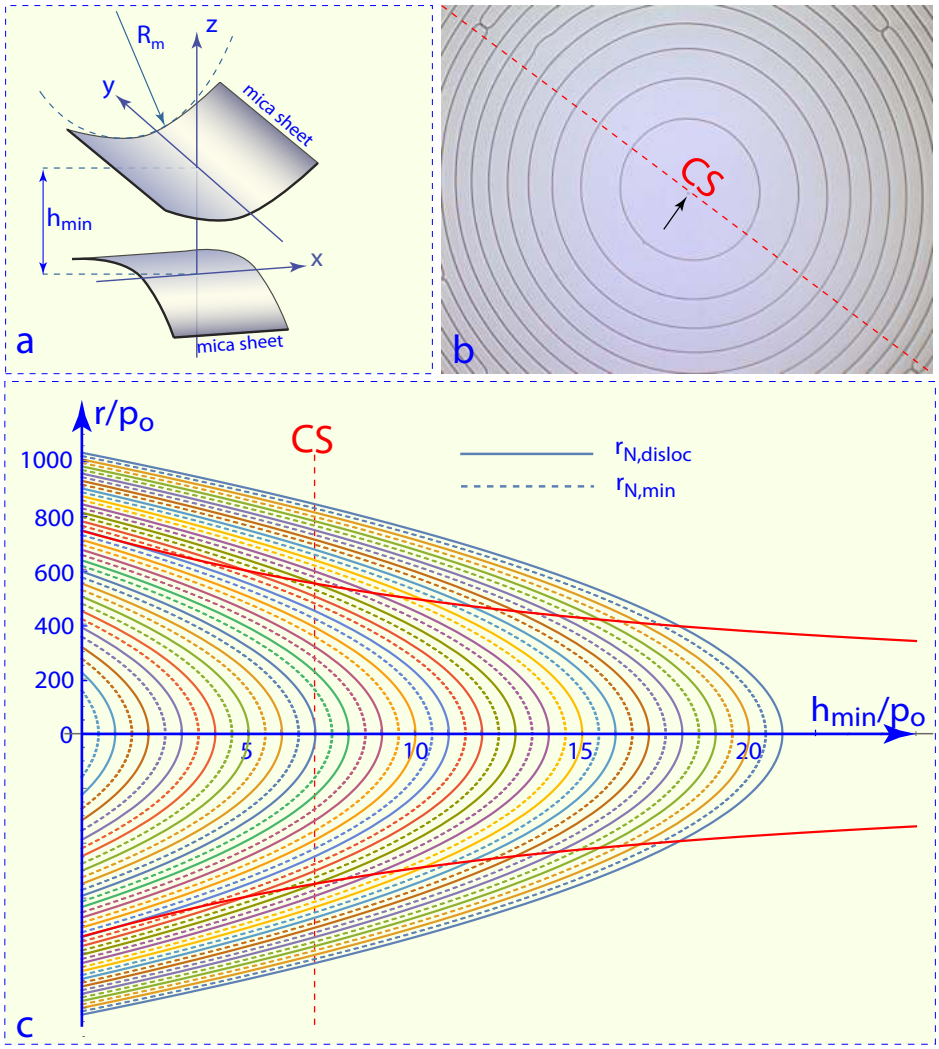

Figure 12: Net of dislocations in the crossed cylinder geometry. a) Perspective view of the setup with crossed cylindrical mica sheets. A circular cholesteric droplet (not shown) is kept by capillarity between the mica sheets. b) Experiment: view a of a net of concentric circular dislocation loops nucleated one after another on the dust particle indicated by the arrow during a slow reduction of the thickness h_{min}. c) Solid lines : plots of the equilibrium radii of dislocations versus the minimal thickness h_{min} calculated in the approximation of vanishing dislocation tension. Dashed lines: plots of radii of circles on which the cholesteric pitch is equal to its natural value p_o.

4 Nucleation and collisions of dislocations in cholesterics

4.1 Setup tailored for manipulation and observation of dislocations

Similarly to the case of monopoles and disclinations discussed above, the issue of generation, motions and collisions of dislocations in cholesterics required elaboration of a special experimental method. The crossed cylinders geometry (see Fig.12a) used in recent studies of cholesteric loops [18, 19] appeared as well adapted for this purpose.

In this setup (see Fig.11), a cholesteric droplet (5CB/CB15 mixture) is confined between freshly cleaved mica sheets providing the planar anchoring. The mica sheets, fixed on supports shown in Figs.11c and d, have cylindrical shapes with the typical radius of curvature $50mm < R_m < 150mm$. The minimal thickness of the gap h_{min} is controlled by means of a micrometric translation stage coupled to a stepping motor.

In this crossed-cylinders geometry, the dislocation lines form concentric circular loops such as those in Fig.12b (the Burgers vector of these thick dislocation lines is $b = p_o$).

4.2 Equilibrium configuration of dislocations in the crossed cylinder geometry

In the approximation of a negligible dislocation tension, the equilibrium radii of dislocation loops are given by

$$r_{disloc}(N, h_{min})/p_o = \sqrt{2R/p_o}\sqrt{N - h_{min}/p_o} \tag{8}$$

where N is the index of dislocations, p_o - the natural full cholesteric pitch, h_{min} the minimal thickness and R - the radius of curvature of the mica sheets. This equation results from the balance of the two opposite forces exerted on the dislocation by the adjacent hypotwisted and supertwisted fields with respectively N and $N + 1$ cholesteric pitches.

In the plot of Fig.12c, the reduced radii $r_{disloc}(N, h_{min})/p_o$ are plotted versus the reduced thickness h_{min}/p_o with solid lines.

In fields with $N - 1/2$ cholesteric pitches, the Frank-Oseen distortion energy vanishes on a circles with reduced radii given by

$$r_{min}(N, h_{min})/p_o = \sqrt{2R/p_o}\sqrt{N - h_{min}/p_o - 1/2} \tag{9}$$

which are plotted versus the reduced thickness h_{min}/p_o with dashed lines in Fig.12c.

4.3 Nucleation and collisions of dislocation loops in supertwisted cholesterics

Nucleation of dislocations loops in supertwisted cholesterics has been extensively studied previously [17, 18, 19]. Here, in Fig.12b we show a system of concentric dislocation loops that were nucleated one after another in the center of the gap during a slow reduction of the minimal gap thickness h_{min}. Nucleation occurred in the gap centre for two reasons.

4.3.1 Elastic energy density in the crossed cylinders gap

The first reason is related to the distribution of the distortion energy inside the gap between the crossed cylindrical mica sheets. Let N be the number of cholesteric pitches in the central area of the gap. The density of the Frank-Oseen distortion energy is a function of the minimal thickness h_{min} and of the radial distance r from the gap centre and can expressed as :

$$f_{el}(N, R/p_o, h_{min}/p_o, r/p_o) = \frac{K_{22}}{2}\left(\frac{2\pi}{p_o}\right)^2\left(\frac{N}{\frac{h_{min}}{p_o} + \frac{(r/p_o)^2}{2R/p_o}} - 1\right)^2 \tag{10}$$

It has been calculated for $N = 20$ and $R/p_o = 25000$ and plotted in Fig.13b. The distortion energy is zero at the bottom of the "energy valley" marked with the dashed line labeled "r_{min}" and given by equation 9. On this line the cholesteric pitch is equal to its natural value p_o. This line divides the energy landscape $f_{el}(h_{min}/p_o, r/p_o)$ in two areas. On the left side of the energy valley, the cholesteric is supertwisted i.e. its pitch p is smaller than the natural pitch p_o while on the right side it is hypotwisted i.e. $p > p_o$.

During the compression of the gap, the maximum of the distortion is located on the ridge of the hill i.e. on the line $r = 0$ corresponding to the gap centre.

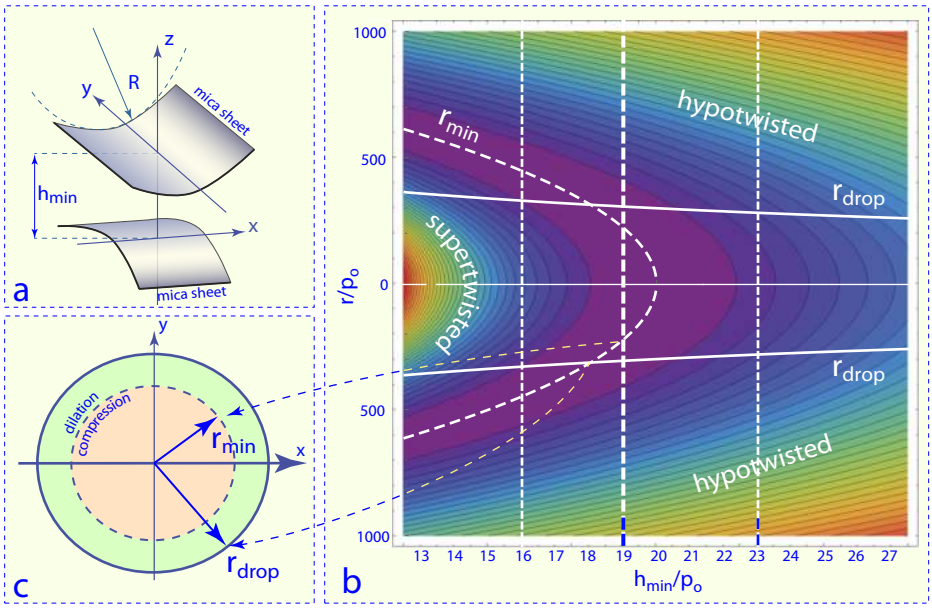

Figure 13: Energy landscape of the cholesteric confined between the cylindrical mica sheets. a) Perspective view of the crossed cylindrical mica sheets. b) Distribution of the Frank-Oseen distortion energy density calculated for a sample containing 20 cholesteric pitches. The energy valley lies between the "supertwist" and "hypotwist" hills. c) Division of the cholesteric droplet into the supertwisted and hypotwisted areas.

4.3.2 Heterogenous nucleation on the dust particles

The second reason for which nucleation of individual loops, one after another, occurred in the centre is related to the presence of the dust particle indicated in Fig.12b by the arrow. Indeed, as pointed out in former studies [18, 19] nucleation of dislocation loops in cholesterics is heterogenous and occurs on surface imperfections or on dust particles.

4.3.3 Collisions of dislocation loops in the supertwisted state

It can happen that in the supertwisted state, nucleation of two dislocation loops, let us say A and B, occurs simultaneously on two distinct dust particles. In such a case, the growing loops A and B will collide. We will postpone discussion of this issue to another paper and here we will focus on another, less evident possibility of collisions of dislocation open dislocation loops nucleated at the meniscus.

4.3.4 Collisions of dislocations nucleated on the meniscus

Let us consider the series of six pictures in Fig.14. The first picture (a) shows a small droplet free of dislocations. It contains 20 cholesteric pitches but its reduced thickness h_{min}/p_o in the centre is only 19 so that it is supertwisted there. From the energy landscape in Figs.13b and c we know that the supertwist stress decreases with r and vanishes at $r = r_{min}$. For $r > r_{min}$ the cholesteric becomes hypotwisted and the stress grows up with r till the meniscus. Upon reduction of the minimal thickness to $h_{min}/p_o = 16$ (see the vertical dashed line in Fig.13b), the whole droplet becomes supertwisted. The next picture (b) shows that in spite of the fact that the elastic stress is maximum in the centre at $r = 0$, nucleation of two open dislocation loops, l1 and l2, occurs at the meniscus because the nucleation barrier is smaller there. The growing loops l1 and l2 collide but as they are located at different levels z, they cross each other (see picture (c)) and continue their way. Meanwhile, as we can see in the picture (d), the third loop l3 appears at the lower border of the drop. In the picture (e) only two loops, l2 and l3 are present. The loop l1 is missing because during his growth it swept the whole area of the droplet and reached the meniscus. The remaining loops l2 and l3 grow and collide. From comparison of pictures (e) and (f) we infer that this new collision l2-l3 is different from the former one l1-l2 discussed above. Indeed, during the collision l2-l3, rewiring of dislocations occurs like in the case of colliding disclinations discussed in the section 3.5. In other words one can say that a coalescence of dislocation loops l2 and l3 took place.

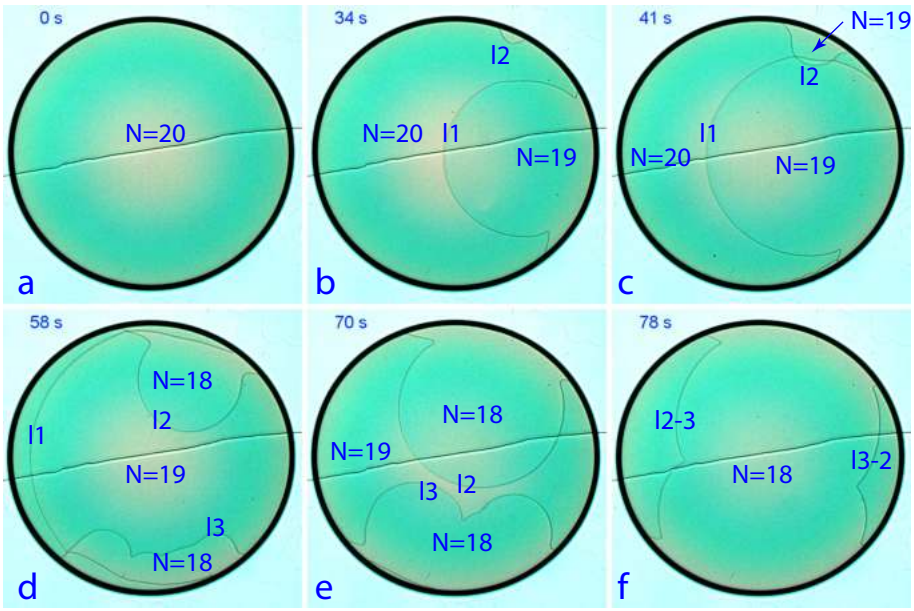

Figure 14: Collisions of open dislocation loops nucleated on the meniscus during compression of the gap. a) Droplet free of dislocations containing $N = 20$ cholesteric pitches. b) Nucleation of two open dislocation loops l1 and l2. c) Intersection of the growing l1 and l2 loops. d-e) Nucleation and growth of the third loop l3. e-f) Collision of loops l2 and l3 leading to the rewiring. (The oblique line corresponds to a step on one of the external surfaces of mica sheets.)

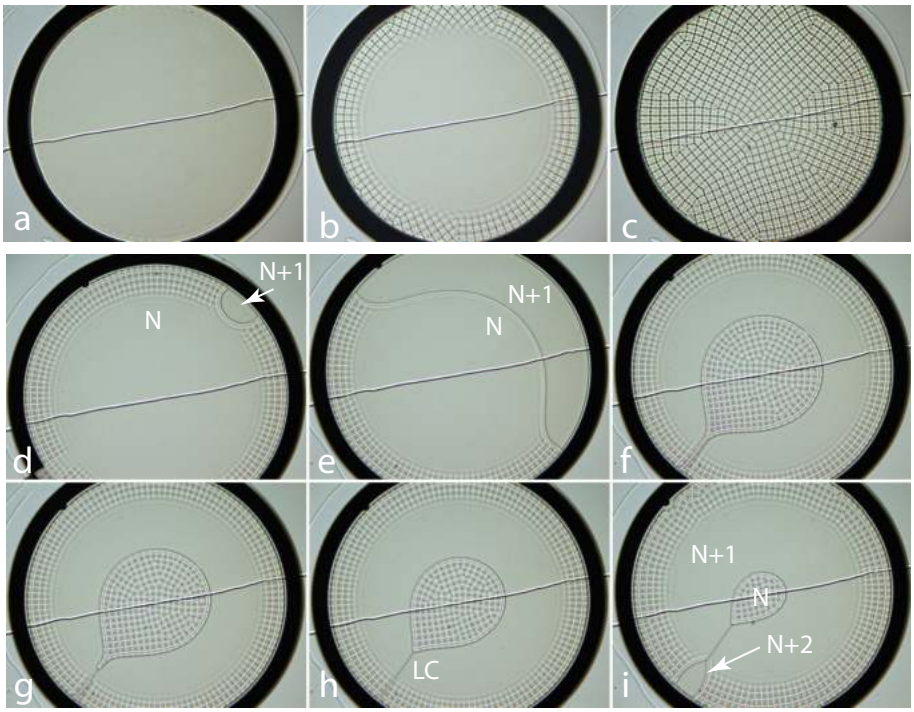

Figure 15: Selfcollision of an open dislocation loop. a-c) Buckling instability in a hypotwisted cholesteric layer containing N cholesteric pitches. d) Nucleation of an open loop inside the buckled area triggered by a transitory radial Poiseuille flow. e) Expansion of the open loop. e-g) Selfcollision of the lateral sides of the open loop. Formation of a pair of dislocations with the total Burgers vector b=0. g-h) Transformation of the dislocation pair into the Lehmann cluster LC. i) Generation of the N+2 field by splitting of the Lehmann cluster. (The oblique line corresponds to a step on one of the external surfaces of mica sheets.)

4.4 Self-collision of one dislocation loop nucleated at the meniscus in the hypotwisted state

To our knowledge, nucleation of dislocation loops driven not by compression but by dilation of the cholesteric helix has not been observed nor discussed so far. The plausible reason for this omission is that in hypotwisted cholesterics, the expected nucleation of loops is preceded by the buckling instability that takes place at relatively small dilation strains.

The buckling instability, hindering nucleation of dislocation loops, occurs also in the crossed cylinders geometry and is illustrated here by the series of three pictures (a-c) in Fig.15. Nevertheless this obstacle can be overcame by application of a short horizontal translation to one of the mica sheets. We have found the resulting shear flow can drive nucleation of dislocation loops inside the buckled state. The dislocation loop shown in Fig.15d has been nucleated by this method.

After nucleation, this loop grows laterally, along the meniscus of the droplet, inside the hypotwisted area partially filled with the buckling instability (see Figs.15d, a and f). Collision of the lateral segments of the loop occurs in Fig.15f. The pair of the adjacent distinct dislocation segments with the total Burgers vector b=0 undergoes a transformation into one thin line corresponding to the so-called Lehmann cluster. The Lehmann cluster is astonishingly stable: it does not split spontaneously upon the further increase of the hypotwist stress (tensile strain). The last picture (i) in Fig.15 shows that nevertheless the Lehman cluster splits when it is submitted to a high enough tensile strain and a simultaneous transitory radial flow. The splitting of the Lehmann cluster into a pair of new dislocation segments leads to generation of a new field containing $N + 2$ cholesteric pitches.

4.5 Collision of two dislocation loops, generation of a topological metadefect; the tangle of dislocations

Collision of two independent dislocation loops (containing N+1 cholesteric pitches) nucleated upon a tensile strain at the meniscus can have two different outcomes:

Crossing When the two dislocation loops A and B are located at adjacent but different levels they expand until they reach the meniscus. This outcome is similar to the one discussed above in the case of dislocations generated by a compressive strain. In microscope such event appears as an apparent crossing of the expanding loops.

Generation of the Lehmann cluster followed by its splitting However, when the dislocation loops A and B are located at the same level (see Fig.1h), their collision leads first to formation of the *Lehmann cluster* (see Fig.16a-b) like in the self-collision discussed above. Upon a further application of a high enough tensile strain (helped eventually by a radial flow), the Lehmann cluster splits at its extremities into two dislocations, situated at different levels (see Figs.16b-c and g-h). For this reason the splitting of the Lehmann cluster driven by the tensile strain can also be seen as *an overlapping transition*. After that, the two dislocations move independently and by this means the splitting of Lehmann cluster progresses.

The total splitting of the Lehmann cluster in Figs.16g-i leads to generation of a tangle because, from the beginning of the splitting, the relative z positions of the dislocations drawn with red and blue lines are different: the red dislocation passes above the blue one on one extremity of the Lehmann cluster and below the blue one on the opposite extremity. If the red dislocation passed above the blue one everywhere two independent loops would be created.

In the experimental example of the generation of the tangle shown in the series of six pictures (a-f) in Fig.16 the tangle itself is hardly visible but one can infer its existence from the motion of dislocation lines hindered by it. The series of six schemes (g-l) in Fig.16 allow to apprehend details of the generation of the tangle.

Upon a continuous action of the tensile strain, the primary tangle winds up into a dextrogyre double-helix of growing height (see Fig.16m-o).

5 Conclusions

This paper on collisions of monopoles, disclinations and dislocations is only a short introduction to a new field that deserves to be explored in more details. The setups tailored for the purpose of generation of topological defects and observation of their collisions should be improved. In particular, the crossed cylindrical mica sheets setup for generation and observation of dislocations in cholesterics deserves some mechanical improvements and the method allowing to control much better the heterogeneous nucleation of dislocations remains to be found.

The most recent result discussed in this paper is the generation of the tangles of dislocations as an outcome of collisions of dislocation loops. We propose to call this peculiar type of tangles *topological metadefects* because they can be seen as defects of topological defects.

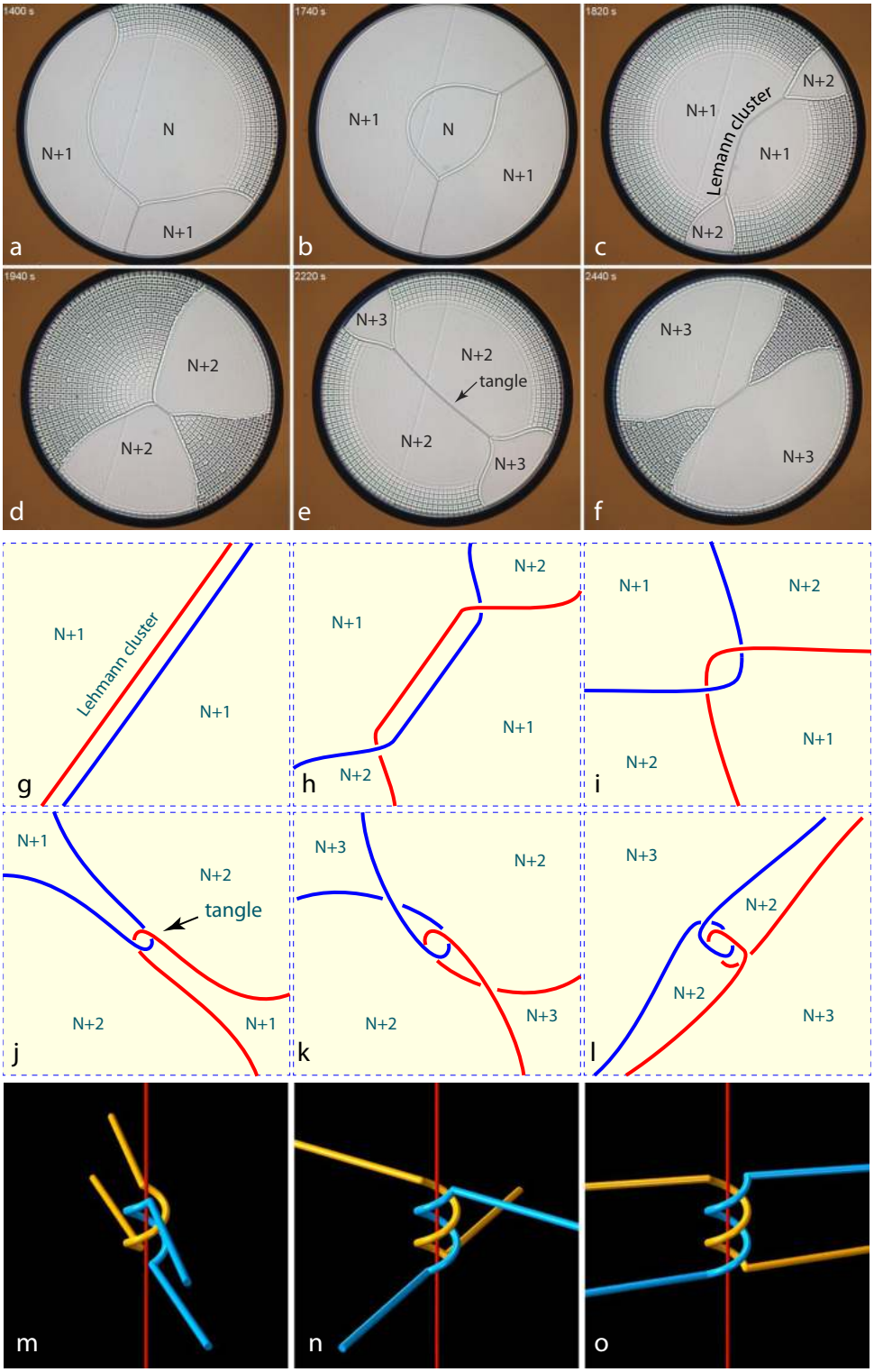

Figure 16: Topological metadefects, tangles of dislocations. a-d) Experiment: generation of the helical tangle by collision of two dislocation in a CB15/5CB mixture. d-f) Beginning of the winding of the double-helix tangle. The tangle indicated by an arrow is hardly visible in these pictures but one can infer its existence from the motion of dislocation lines hindered by it. g-l) Schematic representation of the generation and the beginning of winding of the tangle. m-o) Perspective view of the winding of the double-helix tangle. (see video *Helical tangle* in Supplementary Material)

Otherwise, tangles occur very frequently in Nature as well as in everyday life [21]. For example, tangles of polymeric chains endow the *silly putty* with astonishing visco-elastic properties discussed by P.-G. de Gennes [22].

In the context of Geilo Schools, let us quote as the second example motions of magnetic holes submitted to a rotating magnetic field. Pieranski, Clausen, Helgesen and Skjeltorp [23] have pointed out that their trajectories considered in space-time are entangled.

Acknowledgements

M.H.G and P.P. are grateful to Arne Skjeltorp for invitation to the Geilo School 2022. The authors thank V. Klein, S. Saranga, J. Sanchez, Y. Simon, J. Saen, J.-L. Signoret and M. Bottineau for technical help. We also thank M. Zeghal, P. Judeinstein and C. Goldmann for discussions and help. Rapid progresses in experiments presented here were made during internships of M. Dazza, R. Cabeça, G. Srinivasan, J. Plo, D. Sadi, E. Thellier, T. Alezraa, A. Goré, A.Safi, R. Bouffet-Klein, B. Liagre, and N. Rouger. M.H.G. acknowledges the co-financement by FEDER, European funds, through the COMPETE 2020 POCI and PORL, National Funds through FCT Portuguese Foundation for Science and Technology and POR Lisboa2020 under projects PIDDAC (POCI-01-0145-FEDER-007688, Reference UIDB/50025/2020-2023), Action European Topology Interdisciplinary Action (EUTOPIA CA17139).

Data Availability Statement

No Data associated in the manuscript.

References

[1] T. Ishikawa and O.D. Lavrentovich, Europhysics Lett. **41** 171 (1998) .

[2] I. Chuang, R. Durrer, N. Turok, B. Yourke, Science **251** 1336 (1991).

[3] I. Chuang, B. Yourke, A.N. Pargellis, N. Turok, Phys. Rev. E **47** 3343 (1993).

[4] P. Pieranski and M.H. Godinho, Frontiers in Physics **7** (2020) https://doi.org/10.3389/fphy.2019.00238.

[5] P. Pieranski and M.H. Godinho, Chapter 4 "Physics of the dowser texture" in "Liquid Crystals - New Perspectives", coordinated by P. Pieranski and M.H. Godinho, ISTE - Wiley **2021**.

[6] P. Pieranski and M.H. Godinho, Chapitre 4 "Physique de la texture furcelle" dans "Cristaux Liquides - nouvelles perspectives", coordinated by P. Pieranski and M.H. Godinho, ISTE **2022**.

[7] U. Tkalec, M. Ravnik, S. Čopar, S. Žumer, I. Musevič, Science **333** 62 (2011) .

[8] S. Copar and S. Zumer, Phys. Rev. Lett. **106** 177801 (2011).

[9] S. Copar, Phys. Rep. **538** 1-37 (2014).

[10] I. Musevic, Materials **11** 24 (2018).

[11] H. Agha H. and C. Bahr, Soft Matter **12** 4266 (2016).

[12] M. Dazza, R. Cabeca, S. Copar, M.H. Godinho, P. Pieranski, EPJE **40** 27 (2017).

[13] J. Plot, D. Sadi , E. Thellier, P. Pieranski, M. Zeghal and P. Judeinstein, Am. J. Phys. **89.6** 603-611 (2021).

[14] A. Stieb, G. Baur and G. Meier, J. de Phys. Colloque C1 **36** C1-185 (1975).

[15] J.A. Guerst, A.M.J. Spruijt , C.J. Gerritsma, J. de Phys. **36** 653 (1975).

[16] M. Wang, Y. Li and H. Yokoyama, Nature Comm. **8: 388** 1 (2017).

[17] B. Zappone and R. Bartolino, PNAS, **118.44** e2110503118 (2021).

[18] P. Pieranski, in Memorial Issue of Liquid Crystals Reviews in honor of Maurice Kleman,*Liq. Cryst. Rev.* **86** 1-21 (2021).

[19] P. Pieranski and M.H. Godinho, to be published in Proceedings of the ILCC2022 *Liq. Cryst.* (2022).

[20] F. Grandjean, Comptes Rendus Ac. Sc. **268**, 71–74 (1921).

[21] T.B. Plumb-Reyes, N. Charles and L. Mahadevan, Combing a double helix, *Soft Matter* **18**, 2767–2775 (2022).

[22] P.-G. de Gennes, Entagled polymers, *Physics Today* **36** issue 6, 33-47 (1983).

[23] P. Pieranski, S. Clausen, G. Helgesen, and A. T. Skjeltorp, Braids Plaited by Magnetic Holes, *Phys. Rev. Lett.* **77** 1620-1623 (1996)